A study of Novec 649TM fluid jets injected into sub-, trans- and super-critical thermodynamic conditions using planar laser induced fluorescence and elastic light scattering diagnostics

A study of Novec 649^{TM} fluid jets injected into sub-, trans- and super-critical thermodynamic conditions using planar laser induced fluorescence and elastic light scattering diagnostics

Georgios Kasapis,[1] Shangze Yang,[1] Zachary Falgout,[2] and Mark Linne[1]
[1)]*Institute for Multiscale Thermofluids, School of Engineering, University of Edinburgh*
[2)]*Scania AB*

(*Electronic mail: gkasapis@exseed.ed.ac.uk)

(Dated: 12 September 2022)

This paper describes laser imaging experiments on steady, rotationally-symmetric, laminar jets aimed at observation of the interface between an injected liquid and the surrounding gas under subcritical, transcritical, and supercritical conditions. A steady, laminar flow of fluoroketone enters a chamber of high pressure and temperature nitrogen, allowing direct examination of the interface as it evolves with flow time (i.e. axial position in the chamber). Vapour/liquid equilibrium (VLE) calculations identifying the critical locus for mixtures of fluoroketone and nitrogen are used to define six test cases covering the range from entirely subcritical to entirely supercritical states. Planar laser induced fluorescence (PLIF) and planar elastic light scattering (PELS) imaging are applied to these jets, to image mixture fraction (via PLIF) simultaneous with detection of the interface strength (via PELS). Temperature distributions are acquired using thermocouples. Evidence for the evolution of the interface, and for supercritical states, is presented and discussed.

I. INTRODUCTION

Manufacturers have been developing engines that operate at high combustion chamber pressures and temperatures, generating high efficiency levels and hence low CO_2 emissions. Modern gas turbines can operate with chamber pressures from 20 - 60 *bar*, while Diesel engine chambers can span from 10 - 50 *bar*. Some of these conditions are above the critical point for some fuels, and a subcritical fuel jet could potentially become transcritical once injected. A genuinely supercritical jet in a high-pressure and high-temperature background gas has no surface tension. Evaporation from a subcritical interface is replaced by diffusion through a distributed, supercritical mixing region. Under supercritical conditions, no drops are formed and the fuel jet entrains the surrounding gas more like a dense gas jet.

To add complication, a mixture of compounds will have entirely different critical points (pressure P_c and temperature T_c) than each of the pure substances that form the mixture. The mixture critical point depends on the mixture fractions, and it is not straightforward to estimate, especially if more than two components are present. Fossil fuels have many components and in the main, they may not become supercritical, but planned alternative fuels are similar to single-component fuels, many of them with low critical points, and they are more likely to transition[1]. Moreover, the term "supercritical" denotes an equilibrium state, which may not be reached within the available mixing time in an engine[2,3]. This thermodynamic transition would thus proceed in parallel with mixture formation and combustion.

Supercritical injection is known to occur in rocket motors, where it has been the subject of investigation for some time[3–5]. That case is somewhat more tractable, however, because a pure fluid (e.g. hydrogen) is injected into another pure fluid (e.g. oxygen), with at least one of them already in a supercritical state. Mayer et al.[6] conducted experiments using cryogenic injectants, such as liquid oxygen or nitrogen, into a pressurised chamber. Their data were obtained via single-frame imaging and high-speed cinematography. Their observations revealed mechanistic changes in the way the injectant mixed with the surroundings as the chamber ambient conditions were varied from sub- to super-critical conditions (for conditions relative to the pure injectant). Another commonly cited example of experiments in this regime was published by Chehroudi et al[7]. They injected subcritical liquid nitrogen into a chamber filled with gaseous nitrogen at 300 K [above the critical temperature, $T_c(N_2) = 126.2\,K$]. The chamber pressure was varied from well below the critical pressure to well above it, and they used single-image shadowgraphy to record morphological changes in the jet as they varied conditions. As the pressure was scanned from low to high, what started as a typical turbulent spray transitioned into a dense gas jet when the chamber went above the critical pressure.

Situations involving more complex liquids, like a hydrocarbon, are less straightforward. Dahms and co-workers[8] speculated that in modern diesel engines a supercritical, dense fluid mixing layer no thicker than 30 *nm* would replace the liquid-gas interface across which fuel evaporates, based upon studies of n-dodecane injected into vitiated air. More recently, the high-resolution shadowgrams of Crua et al.[2] for fuel injection into high-pressure and high-temperature vitiated air have become a standard for development of theory. In that work they used a pre-combustion vessel and they injected three different alkane fuels. They performed very high resolution shadowgraphy on droplets that trailed the main injection, after the fuel flow had shut off. Based on high-speed, high-resolution image sequences, Crua et al. developed a conceptual model delineating three droplet regimes: classical evaporation, transitional mixing, and diffusive mixing.

Mo and Qiao[9] performed molecular dynamics simulations using films of the same alkane fuels. They modelled the vaporisation of these fuels in ambient nitrogen under sub-critical

and trans-critical conditions. By using the thermodynamic states recorded and categorised by Crua et al. (either evaporation or diffusion-dominated mixing), they were able to establish a dimensionless transition time for each of these fuels. They did so by plotting contours of the transition time, normalised by the liquid-film lifetime, on pressure-temperature diagrams and noting that a specific contour separated evaporation and diffusion based mixing. The challenge with molecular dynamics simulations is their computational expense, restricting such studies to small geometries (order of nanometers). In an effort to allow comparison with large-scale systems, scaling laws were developed for the fuels studied.

Shadowgraphy is most commonly used to investigate transcritical jets. Harstad and Bellan[10] have argued, however, that shadowgraphy is an inappropriate diagnostic for a transcritical interface because even if it has lost surface tension, the diffusive mixing region will be much thinner than the spatial resolution of an imaging system. The gradient in the index of refraction across that region could produce a shadowgram that has the same appearance as one from an intact interface. Lamanna et al.[11] listed several issues related to high resolution shadowgraphy, and they supported the assertion of Harstad and Bellan.

To quantify transcritical phenomena, a German consortium has studied drops in a high pressure and temperature chamber (see e.g. Lamanna et al.[11] for a review of their work). They have studied a number of fluids (e.g. acetone, n-pentane, n-heptane etc.) using initial drop diameters from 0.8 to 2.0 *mm* released into high pressure and temperature nitrogen. This group has combined shadowgraphy with interface scattering, to overcome the assertion of Harstad and Bellan; scattering was thought to require an intact interface. Lamanna et al. call the technique "front-lighted shadowgraphy", and while using it they observe interface scattering under all conditions investigated (the drop residence time was around 0.5 s). Note, however, that to stabilise and then release a drop requires the fluid to enter at clearly subcritical conditions, to sustain the necessary surface tension. In early work, the same group applied calibrated Raman imaging to the drop wake, to provide some of the earliest quantitative mixing results for fuels under these conditions[12].

In more recent work, Gerber et al.[13] discuss a number of results from a supercritical fuel jet issuing into a shock tube and into a high-pressure, room-temperature chamber. Their jets were highly compressible and turbulent. Their shadowgrams often contained underexpanded jet structures with well-known shock patterns. Gerber et al. applied a laser sheet/elastic scattering technique to image moderately underexpanded jets in the chamber, and they observed elastic scattering from locations that would indicate transitions out of supercritical states, owing to the shock structures. They were localised because following shock structures would return the jet to a supercritical state.

DeSouza and Segal[14] have studied a steady turbulent fluoroketone jet issuing into high pressure and temperature nitrogen, with a nitrogen co-flow. Muthukumaran and Vaidyanathan[15,16] have performed related work with the same liquid, studying various kinds of jets. Fluoroketone is most commonly used as a refrigerant, but it has some useful properties for fundamental studies of thermodynamic interface transitions because it has a low critical point ($P_c = 18.8$ *bar* and $T_c = 169\,^{\circ}C$ in pure form), it is relatively harmless, and it has very high fluorescence yield (i.e. does not require the addition of a fluorescent tracer, which would complicate VLE estimates). Perhaps more importantly, fluoroketone is chemically stable. It will not pyrolyse while under study like most hydrocarbons will. Pyrolysis generates a mix of species which will change the critical properties of the injectant as it evolves. Fluoroketone is also a reasonable thermodynamic surrogate because it has similar properties to the light ends of hydrocarbon fuels (many of the light ends are more likely to transition) and some alternative fuels. Unfortunately, fluoroketone molecules are complex and therefore difficult to model in molecular dynamics simulations.

The fluid interface and its structure play a key role in understanding the transition between a sub-critical and a supercritical fluid mixture. Under engine-relevant conditions, however, neither the internal structure of a transitioning interface nor its evolution during an injection process have been observed experimentally because these features are so small. It is possible, however, to observe macroscopic phenomena whose origins can be linked back to the existence of an interface. For example, Muthukumaran and Vaidyanathan[15,16] monitored axis switching of an elliptical jet, because that process is a function of surface tension. At the critical point, as surface tension disappears, axis switching will cease. In the experiments reported here, the macroscopic phenomenon that was monitored was interface scattering. Elastic scattering from an interface is orders of magnitude stronger than other light scattering processes, such as Rayleigh scattering, and it is linked to the existence of an interface. However, as will be discussed later, monitoring the fluid interface is not sufficient to establish precisely whether a thermodynamic transition to a supercritical state has taken place.

With the above in mind, the goal of the work reported here is to observe the transition of the fluid/gas interface. We study a steady, rotationally-symmetric laminar jet of fluid entering into a high pressure and temperature chamber, because a laminar jet presents a well-defined interface from the moment it enters. This approach also: 1) obviates the need to follow transient drops, 2) allows measurement of local temperature with thermocouples (the system is steady and reproducible), and 3) it allows the liquid to be already supercritical or near-supercritical as it is injected, without the requirement to maintain surface tension at the start. Planar laser induced fluorescence (PLIF) and planar elastic light scattering (PELS) are applied here to provide more quantitative data than simple shadowgraphy provides. We use binary mixtures to simplify estimations of vapour/liquid equilibrium (VLE). In this work we have studied a fluoroketone [Novec649^{TM} by 3M, $CF_3CF_2C(O)CF(CF_3)_2$)] issuing into nitrogen, for the reasons given above.

II. EXPERIMENTAL APPROACH

A. Chamber

The chamber used in this research is depicted in Figure 1. The chamber core is square in cross-section, with sides 73 $\times$ 73 *mm*, and it is 234 *mm* long. The interior is viewed through orthogonal window sets (the fused silica windows are 225 *mm* long, 32 *mm* wide and 20 *mm* thick). The windows are installed in separate steel flanges. Sealing is achieved through the use of o-rings (Barnwell, material: FFKM) that can withstand temperatures up to 300 $^{\circ}C$. Two different gaskets are installed on the interface between each flange and the main body of the vessel. One is made of graphite (novaphit) and provides additional pressure sealing whilst the other is made of phlogopite mica (novamica) and it provides thermal insulation, to isolate the window flange from the chamber body. Each flange is mounted onto the vessel via 28 mechanical, steel fasteners with ceramic washers for further isolation. One of the flanges holds a metal blank, instead of a window, with three feedthroughs (Spectite) that allow thermocouple probes to be placed inside the chamber without breaking the pressure seal. Centred at the top is a capillary tube through which the laminar jet is injected. There are two exhaust channels - one for material in a gaseous state and one for liquid states. Flow through each of these outlets passes through individual throttle (choke) valves, before heading to the exhaust subsystem.

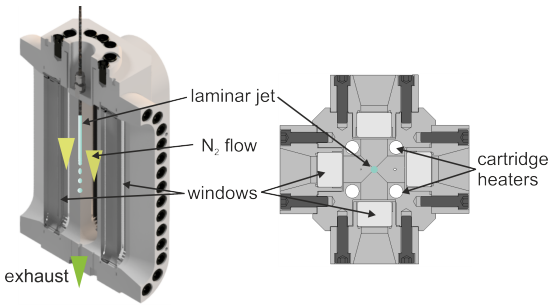

FIG. 1: High pressure and temperature chamber: left - cut-out view, right - top section view.

The vessel is the centrepiece of the experimental setup (see Figure 2) where various subsystems create the desired thermodynamic conditions in the chamber. A flow of high-pressure nitrogen gas is used to control the pressure in the chamber and is heated by four cartridge heaters that span the length of the chamber, but it reaches a peak temperature as it enters at the top. The nitrogen flows steadily and slowly through the heated chamber cavity to the exit at the bottom, together with injected Novec. The chamber pressure depends solely on the mass flow-rate owing to the use of choked-flow exhaust valves. A mass flow controller (Bronkhorst IN-FLOW F-221MI) is used to control the mass flow-rate of nitrogen and thus to stabilise the chamber pressure. The pressure is measured at the output side of the chamber by a pressure transducer (Bronkhorst IN-PRESS P-522CI). Both of these instruments are connected to a Bronkhorst interface device (Flow Bus Terminal E-8501) and they communicate with each other, creating a control system. The nitrogen is delivered to the vessel via four access points located around the perimeter near the chamber top. There is a constant flow of low velocity gas and the mass flow history is logged during each experiment. The chamber pressure is repeatable and very stable during experiments, with fluctuations being limited to within as little as 0.1 *bar*. Pressure is assumed to be uniform within the chamber. The largest Mach number achieved during experimentation is 0.035, well below 0.3; as required to support a uniform pressure assumption.

A piston accumulator serves as the main storage tank for Novec during an experiment. One side is filled with the fluid, initially in a liquid state, and the other side is connected to the same nitrogen gas supply that pressurises the vessel. The supply of fluid to the vessel is controlled by a Bronkhorst mini CORI-FLOW^{TM} M14 mass flow-rate controller. The fluoroketone mass flow rate is set to 900 gm/hr. The pressure at the supply pressure regulator, which is used for both the accumulator and the nitrogen mass flow-rate controller, is typically held at 20 bar above the required chamber pressure. The liquid flows through a 0.8 *mm* diameter stainless steel tube that is 102 *mm* long (ensuring fully developed laminar flow) and it enters on centre-line at the top.

The nitrogen flows slowly through the chamber to clear out vapour steadily, but it presents a relatively quiescent gas to the liquid stream. We have confirmed that under steady conditions, fluoroketone vapours do not build up in the chamber because: 1) PLIF images of fluoroketone vapour do not indicate changes with time, and 2) the mass flow rate of nitrogen required to maintain the set chamber pressure remains constant.

The fluid injection temperature is controlled by a separate heating system. A flexible rope heater is wrapped around the final section of the fluid delivery tube. A control thermocouple (K-type) measures the fluid temperature and communicates this to a PID controller (Omega engineering CN742) which in turn supplies power to the rope heater via a solid-state relay.

The control thermocouple probe is constantly present at the side of the fluid flow, about 15 *cm* upstream of the nozzle exit. Flow disturbance caused by this thermocouple quickly dies away and the fluid is delivered in a laminar state. To avoid heat loss in the section past the control thermocouple, an insulated portion of the rope heater extends beyond the control sensor. The temperature at the nozzle output was measured by bending one of the chamber thermocouples to that position and calibrating the temperature controller to achieve the desired injection temperature at the nozzle exit (that thermocouple was removed when imaging the jet). The calibration process was done under all the test cases reported in Table I.

Cartridge heaters are embedded in the vessel and are used to heat the main body and interior. The thermocouple (K-type) used for the temperature control system is embedded in one of the four heaters and sends a signal to a National Instruments (NI) C Series Temperature Input Module. This, in turn, sends the temperature reading to a LabView programme located on the main desktop PC where a PID controller adjusts cartridge heater output accordingly. The temperature inside the cham-

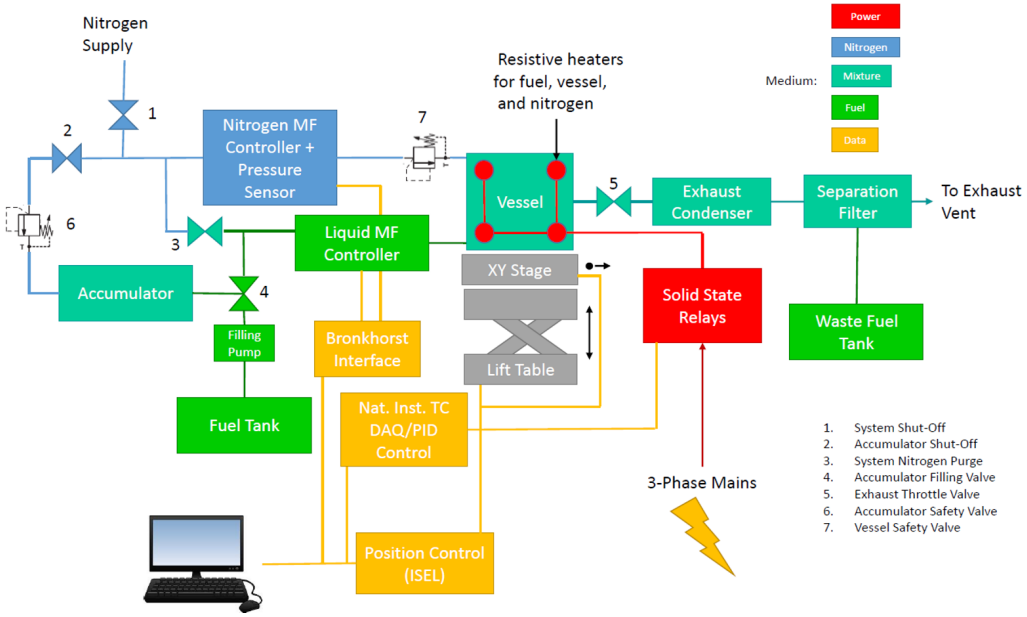

FIG. 2: Diagram of the experiment

ber is measured using three K-type thermocouples (omega Engineering, KMTSS-IM100E-150) with exposed junctions. These are spaced in the vertical direction, in the jet plane, and are located at 40, 102.5 and 165 *mm* below the nozzle outlet. The thermocouple probes are flexible, allowing the measurement location to be varied.

The PID control set-points were calibrated so that they would produce the desired chamber temperature reading at the first thermocouple. The chamber conditions were repeatable for each case to within a degree. The body of the vessel is insulated with glass fibre foam and, prior to fluid injection, the chamber temperature is uniform once steady state conditions are reached. Temperature profiles taken inside the chamber using thermocouples (without a fluoroketone jet) indicate that the chamber gas temperature falls linearly with vertical distance, by 0.2 K/cm. The radial temperature profiles are flat to $\pm 2.1K$.

Control of the chamber's physical location, relative to the static optical diagnostic system, is achieved by use of two separate systems. A motorised lift table, upon which the vessel sits, can be used to change the chamber elevation. A displacement sensor (iGaging Absolute Origin DRO) measures changes in elevation. Movement in the horizontal plane is made possible through an x-y stage and controlled via an ISEL step controller (iMC-S8) through a software interface (ISEL PAL-PC).

B. Fluoroketone thermodynamics

For pure Novec (the fluid is in pure form inside the delivery system up to the nozzle exit), $P_c = 18.8$ *bar* and $T_c = 169\,^{\circ}C$. The boiling point for pure Novec at 1 *bar* is $T_{bp} = 49\,^{\circ}C$. In the last few *cm* of the liquid delivery system we heat the fluid well above that temperature, but it is delivered at 16, 19, or 31 *bar* (depending on the experimental test case), and we detect no evidence for boiling inside the delivery system. Once inside the chamber, however, the liquid can evaporate. Evaporation is a common, interfering issue for transcritical fluid experimentation.

In order to develop experimental conditions for this study, it is necessary to understand vapour liquid equilibria (VLE) for fluoroketone/nitrogen mixtures in the chamber, which then identify the critical points for various mixture fractions (the critical locus).

There are numerous equations of state (EoS) available for predicting the vapour-liquid coexistence region of binary mixtures. Two such EoS include the Peng-Robinson and PC-SAFT models. Linnemann and Vrabec[17] used a view cell to detect the critical locus for Novec/N_2 mixtures by observing the disappearance of the liquid/gas interface at specific pressures and temperatures, for various mixture fractions. They then compared the performance of the Peng-Robinson and PC-SAFT models for the mixtures they had observed, and they reported that the PC-SAFT model matched the experimental data more closely. PC-SAFT is an equation of state that models molecular interactions. For pure fluid modelling purposes, three substance-specific parameters are required. These include the segment diameter, segment energy parameter, and the number of segments per chain. To calculate VLE states of binary mixtures, these parameters are supplemented with a binary interaction parameter that can be calibrated using experimental data.

To establish conditions under which vapour and liquid cannot co-exist within the chamber, it is useful to identify the critical locus on a graph of pressure against temperature. Here the commercial software FluidProp^{TM} was used to calculate VLE states. FluidProp can execute the calculations with a num-

ber of different models, including PC-SAFT. VLE calculations can be highly non-linear, however, and it is good practice to replicate experimentally obtained data in order to validate the code's performance. In personal communication with the company developing FluidProp, the PC-SAFT model parameters for Novec 649 were updated to match the ones reported by Linnemann and Vrabec[17]. Following this update, agreement between the model and the data was good, as illustrated in Figure 3. Unfortunately, the program struggled to calculate the bubble line for part of the composition range (mole fraction of nitrogen from 0.4 to 0.7). Despite not being able to calculate VLE states for all of the compositions, the model was able to predict bubble-point pressures correctly up to nitrogen mole fractions of 0.4 for all cases, and the agreement with experimental data was near perfect in that region. Additionally, in the case of the 420 K isotherm, which is closer to the temperatures of the experimental cases in this work, the prediction is close at the critical point as well. The inaccuracy appears to be lower at higher temperatures, with the worst error being at the lowest (360 K) isotherm where the critical pressure was over-estimated. The highest predicted VLE pressure occurs at the 360 K isotherm and is just over 200 *bar*, in agreement with the PC-SAFT prediction reported by Linnemann and Vrabec. For the 360 K and 390 K isotherms, VLE is possible beyond a nitrogen mole fraction of 0.7 and the model predicts the maximum value of concentration for VLE to be approximately 0.9 and 0.8, respectively, which is also in agreement with what was reported[17].

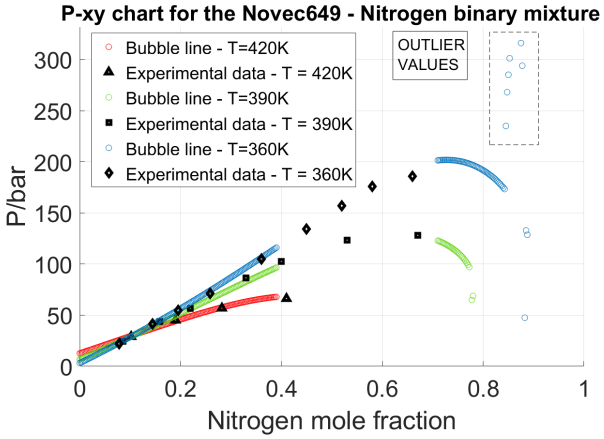

FIG. 3: Novec/N_2 phase envelopes at various isotherms presented as pressure against mole fraction of nitrogen plots, supplemented with experimental data published in[17].

FluidProp was then used to generate the P-T diagram depicted in Figure 4. The results indicate a rapid increase in the critical pressure as nitrogen is added. Nitrogen has this effect on the critical pressure when it is combined with many fluids. In contrast, the critical temperature of the Novec/N_2 mixture gradually decreases as nitrogen is added.

There are various statements in the literature on supercritical states. For a pure substance, most authors agree that it is necessary to be above both P_c and T_c[18], which certainly was the case in the pure nitrogen experiments by Chehroudi

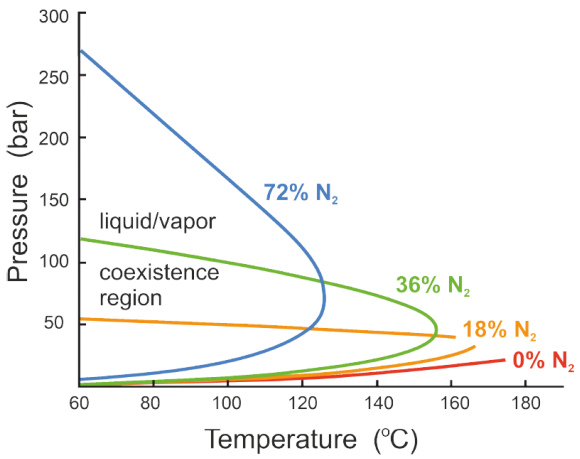

FIG. 4: VLE curves for Novec/N_2 mixtures.

et al.[7]. Some authors assert that if a binary fluid mixture is above P_c *or* T_c, it is supercritical[19]. Others chose to divide the pressure-temperature map into finer blocks with more detailed descriptions[20]. The results in Figure 4 indicate that all mixtures of interest would fall outside the coexistence region if we hold temperature at or above 175 $°C$. Note that for a mixture with 72% N_2, the critical pressure is around 265 *bar*, a pressure we cannot reach experimentally. The mixtures we study at $T_{\text{chamber}} > 175\,°C$ might therefore be called "gas-like supercritical" by some, although for type-III binary mixtures (using components that have well-separated critical points) even that description is oversimplified[21]. For notation, we will call that regime "supercritical", but our main point is that the condition lies outside the coexistence region in Figure 4 while remaining near the Widom line in Figure 5 (as discussed further below).

Six experimental test cases were defined for this project, based upon FluidProp VLE estimates and some initial experiments. The test cases are presented in Table I.

Reduced temperatures (T_r) and pressures (P_r), defined by $T_r \equiv T/T_c$ and $P_r \equiv P/P_c$, are often reported in the literature. For the binary mixtures in this study, T_r and P_r depend on Novec mixture fraction and hence position in the chamber, so they are not reported here. Table II contains the reduced temperatures and pressures for pure Novec inside the nozzle, for all six test cases.

The Widom line can be thought of as an extension of the coexistence line for a pure substance (the 0% N_2 line in Figure 4) into the supercritical region. The location of the Widom line on a pressure/temperature plot is typically defined in terms of maxima in the constant pressure specific heats (C_p)[22]. Here we have used FluidProp to estimate the locations of C_p maxima for pure Novec as a function of pressure and temperature. The result is plotted in Figure 5, on which we have also plotted test case points (from Table II) for pure Novec inside the nozzle, together with chamber conditions (purely for reference). When the thermodynamic state of a substance crosses the Widom line, a non-linear transition occurs. The inset in Figure 5 shows the variation of C_p with temperature, at sev-

TABLE I: Experimental test cases. On a day-to-day basis, feedback-controlled liquid temperatures are reproducible to $\pm 0.1\,^{\circ}C$, gas temperatures are reproducible to $\pm 1\,^{\circ}C$, and pressure is reproducible to $\pm 0.1\,bar$.

Test case	T_{Novec} ($^{\circ}C$)	T_{chamber} ($^{\circ}C$)	P_{chamber} (bar)	Description
1	160	150	16	Subcritical jet into subcritical chamber
2	190	150	16	Superheated vapor ($T > T_c$ but $P < P_c$ inside injector) into subcritical ($T_{\text{ch.}} < 170\,^{\circ}C$) chamber
3	170	170	19	Critical point ($T_c \,\&\, P_c$ inside injector) into critical point ($T_{\text{ch.}} = 170\,^{\circ}C$) chamber
4	160	220	16	Subcritical (inside injector) into supercritical ($T_{\text{ch.}} > 175\,^{\circ}C$) chamber
5	160	220	31	Compressed liquid ($P > P_c$ but $T < T_c$ inside inj.) into supercritical ($T_{\text{ch.}} > 175\,^{\circ}C$) chamber
6	190	220	31	Supercritical ($P > P_c$ and $T > T_c$, inside injector) into supercritical ($T_{\text{ch.}} > 175\,^{\circ}C$) chamber

Note: pressures reported here are absolute pressure. T_{chamber} is measured by an off-centreline type K thermocouple located 40 *mm* below the nozzle exit.

TABLE II: Reduced temperatures and pressures for pure Novec inside the nozzle, for the test cases in Table I.

Test case	T_{Novec} ($^{\circ}C$)	T_r	P (bar)	P_r
1	160	0.98	16	0.85
2	190	1.05	16	0.85
3	170	1.00	19	1.01
4	160	0.98	16	0.85
5	160	0.98	31	1.65
6	190	1.05	31	1.65

eral relevant isobars both below and above the critical pressure of pure Novec. The temperatures at which the C_p maxima occur (at supercritical pressures) correspond to points on the Widom line. To cross the Widom line from left to right is termed "pseudoboiling". According to Banuti[23], beyond a supercritical pressure of $P/P_c > 3$, C_p maxima can, in general, be expected to have completely decayed and pseudoboiling effects become negligible. This is reflected in the fact that the C_p peak at the 31 *bar* level, depicted by the inset in Figure 5, is significantly less pronounced than the peak at the 19 *bar* level.

The highest reduced pressure achieved here was $P_r = 1.65$ (for cases 5 and 6). For case 6 especially, pseudoboiling effects are not negligible and should be considered because the injection conditions of the pure fluid are in the vicinity of the Widom line. The injectant conditions under test cases 1, 2 and 4 are at sub-critical pressures. In test case 5 the reduced pressure is $P_r = 1.65$ but the injection temperature is low enough that no pseudoboiling effects would take place (see the C5 point in Figure 5). Under test case 6, however, the injectant exists at a state that is very close to the Widom line. At 31 *bar*, the pseudoboiling temperature, T_{pb}, is estimated to be $192.4\,^{\circ}C$ and the injection temperature is $190\,^{\circ}C$. The injection temperature will be subject to fluctuations, however, and there is an error associated with estimating T_{pb} via an equation of state. Furthermore, the lower C_p maximum at elevated supercritical pressures is accompanied by a broadening of the C_p curve, meaning pseudoboiling effects can be expected at that condition since they take place over a larger range of temperature. As will be discussed later, this is one possible reason for a detected drop in temperature during injection under test case 6.

Test case 3 is unusual because of a critical point overestimation by the PC-SAFT equation of state. FluidProp considers 19 *bar* to be a sub-critical pressure for pure Novec (it estimates the critical pressure to be 21.39 *bar*). Furthermore, it should be noted that the blue C_p curve in the inset plot of Figure 5 indicates the drop in C_p that FluidProp estimated should take place across its predicted coexistence line; not the Widom line. Nevertheless, in case 3 Novec is considered here to be injected under a near-critical (slightly supercritical) state compared to the published critical point. Owing to the close proximity to the critical point, large fluctuations in various thermophysical properties could be expected.

In addition to the cases in Table I, we conducted a short experiment to identify changes in the axial location for a clear loss of interface, together with the rate of transition. Here, a subcritical jet (at $T_{\text{Novec}} = 160\,^{\circ}C$) was injected into chamber pressure of 16 *bar* and temperatures of $T_{\text{chamber}} = 180\,^{\circ}C$, and $200\,^{\circ}C$ (called test cases 1a, and 1b). These two cases fill the T_{chamber} gap between cases 1 and 4 (all at $P_{\text{chamber}} = 16\,bar$), so we combine all four cases in this smaller study.

C. Planar laser-induced fluorescence (PLIF) and planar elastic light scattering (PELS)

DeSouza and Segal[14] have explored the photophysics of fluoroketone in detail. It can absorb laser radiation at the third harmonic of Nd:YAG (355 *nm*), but that wavelength is near the edge of the absorption spectrum. The fluorescence spectrum peaks near 420 *nm*. The absorption and emissions spectra touch in the wings but do not strongly overlap; radiative trapping of the fluorescence is not a major issue.

The optical setup for this study (depicted in Figure 6) monitored fluorescence and elastically scattered light signals simultaneously. The output of a Quantel pulsed Nd:YAG laser in the third harmonic was spread into a sheet using three cylinder lenses. The vertical dimension (40 *mm*) was set by a 50 *mm* focal length cylinder lens followed by a 500 *mm* focal length cylinder lens (both lenses with their cylinder axes oriented horizontally). A $\sim 7.9\,mm$ thick sheet was established by a third 750 *mm* focal length cylinder lens (with its cylinder axis oriented vertically).The sheet thickness was measured using a WinCamD (DataRay Inc) after the sheet had passed through the input window. Given the width of the sheet, the entire jet was illuminated (at the nozzle the jet is 0.8 *mm* in diameter).

The PLIF/PELS imaging system used a 2 inch dichroic mirror in front of the exit window, reflecting 355 *nm* light to

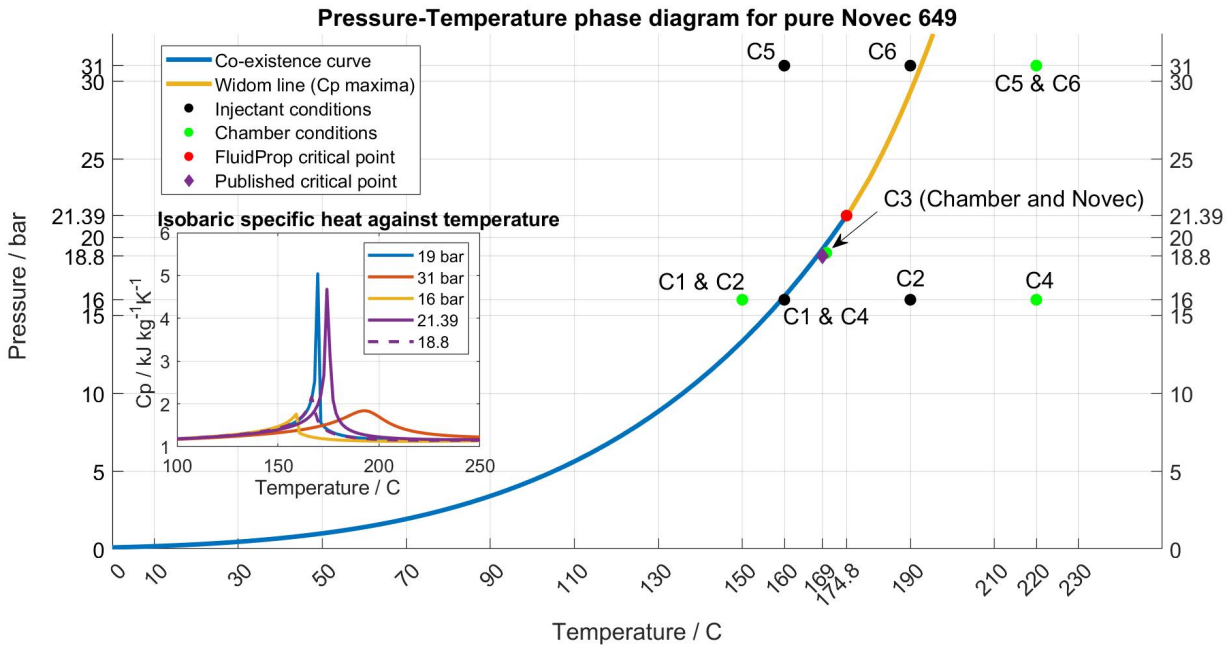

FIG. 5: Pressure-Temperature phase diagram for pure Novec 649, showing the coexistence and Widom lines, both calculated using FluidProp^{TM}. Both the injectant and chamber conditions have been marked using filled markers. Test cases have been indicated adjacent to these with the letter "C" followed by the test case number. The inset figure depicts the variation of the isobaric specific heat capacity, C_p, with temperature at relevant pressure levels.

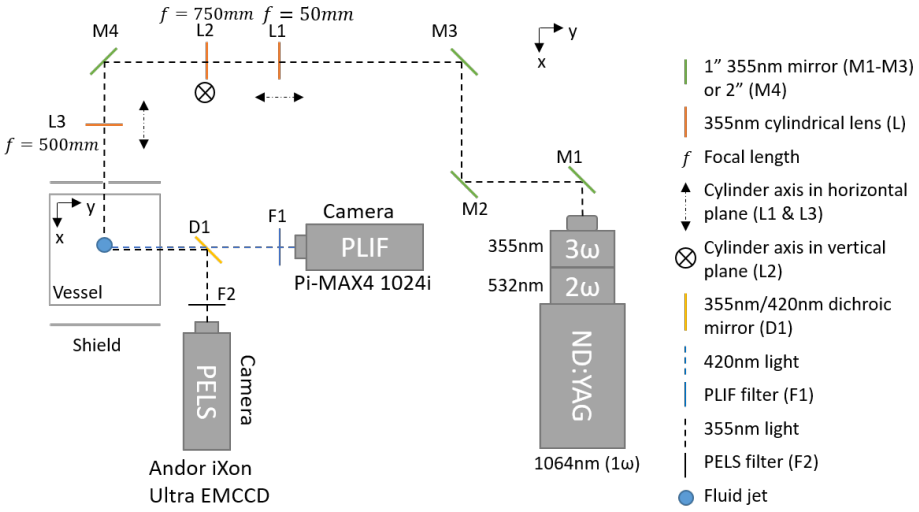

FIG. 6: Combined PLIF and PELS optical setup

an Andor iXon Ultra EMCCD camera (used for PELS) and passing fluorescent light to a Princeton Instruments Pi-MAX4 1024i camera (for PLIF) equipped with a bandpass filter centred at 420 *nm* and a bandwidth of 10 *nm* FWHM. The Andor camera was fitted with a 50 *mm* focal length lens while the Pi-MAX was fitted with a 105 *mm* focal length lens. The camera images were registered to each other, but since the imaging chips have different dimensions, the exercise only ensured that we viewed the same field at similar magnification. Distances were calibrated for both cameras by imaging a high resolution ruler located in the image plane. PLIF/PELS images presented here were taken on the jet centre-line.

We rely upon linear fluorescence (at 60 *mJ* per pulse, linearity was confirmed by measurement) because we did not detect problems with optical depth in our initial experiments, and linear fluorescence makes scaling more straightforward. We assume the fluid exiting just at the nozzle is 100% Novec, while 0% is the background level acquired during every exper-

iment. We also assume that fluorescence is linear in number density. The 100 PLIF images per test case and location were background subtracted and corrected for the laser sheet profile, which was acquired by imaging the sheet using surface scattering from a uniform, non-fluorescing card.

The sheet of laser light at 355 *nm* will also scatter elastically from an intact liquid interface. This signal can be used to detect when the interface is strong, when it is weakening, and when it has disappeared. Loss of interface scattering could be caused by a supercritical transition or because the liquid has vaporised entirely; this measurement alone is not sufficient to decide whether the fluid has become supercritical, but it is a contributing piece of information.

Because the subcritical jets are not optically thick, the laser sheet entered and was reflected around inside the liquid before exiting towards the camera. The camera collected image signatures of randomly varying caustics for that reason. Despite their complexity, caustics contain evidence for interface scattering. Because the jet underwent Rayleigh breakup when surface tension was present, small wave structures were developed across the interface and these structures located the strongest caustics. Under subcritical conditions, however, the Novec was vaporising so the liquid column shrank over time even in that case.

To analyse these data, we acquired 200 elastically scattered images, subtracted the background from each, normalised each of them for the laser sheet profile, and then averaged all 200 images. We then averaged each radial signature at each axial position to give an averaged scattering signal as a function of axial position.

Koller et al.[24] have demonstrated that one can infer surface tension from single-surface scattering measurements. That calculation is not appropriate in this case, however, because there are several reflections involved in the production of the PELS signal, and at each axial location it is not possible to know how many were involved. Moreover, we have recently demonstrated that a diffuse interface, typical of the predicted interface for a transcritical jet, retains some reflectivity[25]. Reflectivity does not instantly become zero when the interface begins to degrade. For Novec, as an example, the reflectivity of a 50 *nm* thick diffuse interface (with nearly zero surface tension) can be around 0.055, and it doesn't reach zero until the interface is roughly 150 *nm* thick. In comparison, the Fresnel reflectivity for an infinitely thin Novec/N_2 interface is 0.075, which is only about 40% larger than diffuse-interface reflectivity. Once a transcritical interface begins to break down, it would no longer be possible to infer surface tension using the formalism presented by Koller et al. The fact that a weakened interface maintains reflectivity, however, explains some of our weakened PELS results.

D. Magnified PLIF

Following the PLIF and PELS experiments, a second campaign was conducted. Magnified PLIF (MPLIF) imaging with improved spatial resolution and greater magnification factor provided more detail on Novec distributions.

The optical setup for MPLIF was similar to the previous setup. The only difference was that the PELS signal was not monitored, so that the dichroic could be removed and the camera moved closer. Here, the Andor camera was used to acquire the MPLIF images (for improved spatial resolution). To improve the magnification factor macro-tubes increased the distance between the image sensor and the 105 *mm* focal length Nikon lens. As the camera was moved closer to the object, the depth of field was expected to be smaller. Since the laser sheet has a finite thickness, a portion of it might have extended beyond the depth of field. To avoid collecting out-of-focus fluorescent light contributions, a mechanical slit was used to ensure the laser sheet was narrower than the depth of field (the sheet had a width of 3.9 *mm* measured with a WinCam at the imaging location). The laser light sheet was thicker than the jet at the nozzle exit (with a diameter of 0.8 *mm*). Even in this case, therefore, the laser excitation and fluorescent emission were volumetric.

The original PLIF images (Figures 9 to 14 below) did not indicate significant absorption of laser light as it traversed the jet, and so a laser energy level ensuring that the LIF signal fell into the linear regime was chosen. Linear LIF offers advantages in terms of scaling, and in this work the data are scaled.

The magnified PLIF images, however, contained evidence for absorption of the laser beam (approaching from the left in the MPLIF images below). As an example, in the top of the transient image of Figure 16d, a decrease in LIF signal can be detected on the right hand side. This issue existed primarily in the dense jets near the nozzle outlet. Despite the fact that absorption was an issue only for a small region of some flows, we developed a scheme for correcting data starting from the nozzle exit, to render all of the results more useful.

Our approach to correction was developed using images that were averages of 100 individual MPLIF images, and it consisted of several computational steps. It was first necessary to model the loss of laser irradiance via absorption as it passed across the jet, and then to infer the effect of this diminished irradiance on the local LIF signal.

Loss of irradiation as it passes across a non-uniform distribution of mass requires application of the equation of radiative transfer (ERT). The more commonly used Beer's law does not apply in this case because it was developed assuming a uniform mass distribution. For continuous functions, absorption is modelled in the ERT using[26]:

$$I(x) = I(0)\mathrm{e}^{-\tau(x)\cdot x} \tag{1}$$

where $I(x)$ is the laser irradiance (W/m^2) as a function of radial position x, $I(0)$ is the input irradiance, and τ is the optical depth defined by:

$$\tau(x) \equiv \int_0^x N(x')\sigma dx' \tag{2}$$

where $N(x')$ is the mass distribution written in the form of absorber number density, and σ is the absorption cross-section (m^2). For discrete data, such as we have acquired, the integration in equation 2 is replaced by a summation, with discretisation performed on a per-pixel basis.

To model LIF rigorously, based on $I(x)$, requires the solution of coupled rate equations, and the outcome can be highly uncertain. Instead, we assert that LIF is linearly proportional to $I(x)$ (the LIF excitation source). It is then possible to normalise the experimental LIF profile at a specific axial location and compare it to a normalised value of $I(x)$ (from equation 1), since there is a direct proportionality. Once the two match, the form of $N(x')$ used in equation 2 then provides the profile for mass distribution which can be scaled to the actual density.

We modelled the density profile $[N(x)]$ using a super-Gaussian function:

$$N(x) = N_{\text{peak}} \exp[-(x-b)^2/(2c^2)]^P \tag{3}$$

where N_{peak} is the number density at the peak of the function, b can be used to offset the curve centre from 0 (an issue for the jets farther downstream because the jets were not perfectly vertical), c controls the width of the distribution, and P controls the shape of the curve. Example super-Gaussian curves are shown in Figure 17 below, where the density curves near the nozzle represent a nearly top-hat profile and curves farther down in the flow (axial distances 5 and 7 *mm*) represent a Gaussian shape. We justify this functional dependence, for application to the averaged images, by the fact that the experimental curves have these same profiles on the laser input side up to the point where absorption distorts them. Moreover, other sources (see e.g. the Raman imaging results by Mayer et al.[27]) indicate that a jet like this one will exit the injector tube with a nearly top-hat density profile and it will evolve into a Gaussian profile with axial distance.

The MPLIF image correction process started at the nozzle outlet, which is a reference point because the distribution at that location was a nearly top-hat profile of pure Novec, with negligible amounts of vapour to the side. The wings of the normalised LIF distribution at that point were used to fit an initial super-Gaussian (fitting c and P). At the nozzle outlet b was set to 0. The inferred $N(x)$ distribution was then used in equations 1 and 2 to infer a normalised LIF signal. The error between the simulated LIF profile and the measured profile (both normalised to their peak values) was then minimised by adjusting c and P. Here, σ was also allowed to float because the laser sheet was thicker than the jet at the nozzle, meaning that the absorption path length varied from the jet diameter on centre-line to nearly zero in the vapour that existed well beyond the edges of the jet. The σ values inferred using this technique were significantly lower than the various published values for this reason (for liquid $0.23 \times 10^{-20}\,[cm^2/molec]$[28] and for vapour $38.1 \times 10^{-20}\,[cm^2/molec]$[29]), but the difference occurs because we use σ to account for path length variation.

There is no cross-talk between c, P and σ during minimisation because c can be set using both sides of the experimental LIF curve, P sets the width of the top of the profile, and σ controls how much the LIF signal decreases with distance across the distribution.

This minimisation process generated a normalised expression for $N(x)$, which was then set on an absolute mass basis using the density of Novec at the nozzle outlet, as estimated by FluidProp. This result was checked against the known mass flow rate for Novec and the maximum error was 15.4%. The disagreement, which is one indication of the uncertainty in the correction, is a result of several factors. First, FluidProp is not entirely accurate (none of the EoS are). For example, it disagrees with the published critical temperature for pure Novec by 3.4% and with the critical pressure by 13.8%, overestimating in both cases. Next, the PLIF image near the nozzle outlet is generated by a cylindrical volume of fluid because the laser sheet illuminates the entire jet. The centre of the jet generates an LIF signal across the entire diameter while the edges generate LIF from thin regions, meaning that the centre is somewhat over-emphasised relative to the edges. These issues decrease in importance with distance downstream because the laser sheet is no longer absorbed strongly and the jet becomes wider. Uncertainties will be discussed in more detail below.

A similar process was used to extract density profiles $[N(x)]$ at downstream axial locations. Optimising b for the downstream data helped to avoid erroneous narrowing/broadening via c to account for centre-line mismatch, and it prevented non-physical solutions whereby the code would raise the signal level and apply strong absorption to achieve a better fit, precisely because of misalignment of the curve centres. Finally, the absolute mass density was inferred by scaling the downstream distribution with the LIF signals.

E. Temperature measurements

Temperature measurements were performed using thermocouples to acquire temperature maps in the injection plane. Because the flows are steady and reproducible, three thermocouples inside the chamber were used to measure the temperature at various locations. To vary the test location, the probes of the thermocouples were bent and their location monitored via images from a spatially calibrated camera looking directly at the jet plane (i.e. placed perpendicular to the plane). To ensure the thermocouple bead (approximately 0.5mm in diameter) was in the jet plane, a second camera was used to view it end-on and the probe was rotated until the bead was seen to be on the centre-line of the injection nozzle. Radial and axial profiles of temperature were obtained.

III. EXPERIMENTAL RESULTS

A. PELS results

The PELS images were analysed as described above, and Figure 7 includes the results for the six test cases provided in Table I. The images were corrupted by scattering from the nozzle within the first few *mm*, so the PELS data start at 2.5 *mm* below the nozzle outlet. In Figure 7, one can see that there is a significant interface scattering signal for cases 1, 4 and 5. These three cases use the same temperature for the injected liquid, and it is below T_c for the pure liquid. The oscillations in cases 1 and 5 were repeatable; they were established by the

wave structure in the liquid column. These wave structures, which are characteristic of the Rayleigh breakup process, are an indication that surface tension remains significant, but the structures are less pronounced in case 5 than they are in case 1. Case 4 did not have such strong wave structure or oscillations. The difference between cases 4 and 5 is that case 5 was at almost twice the pressure of case 4. The jet was therefore more dense and it had a higher boiling point. The test case 1 curve has two slopes, with a steeper slope between 2.5 and 12 *mm* axial distance, and a reduced slope afterwards. This happened because the average intact liquid length for that jet was 12 *mm*. Past that point, gaps between drops reduced the slope of the averaged curve. Note that the curve for test case 5 does not have the same change of slope, and the magnitude between 2.5 and 12 *mm* axial distance is fairly low compared to case 1, implying a weakening of the interface.

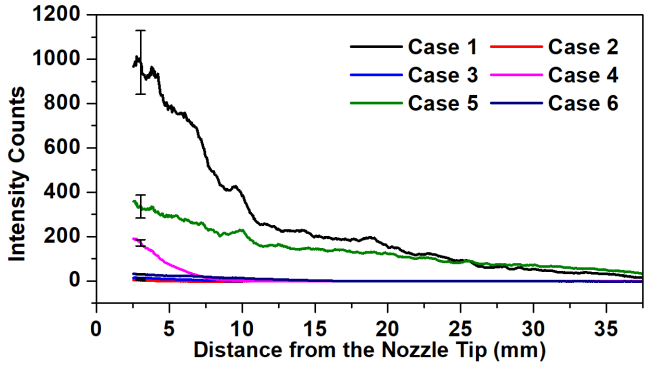

FIG. 7: PELS results for the jets under the test cases listed in Table I. The average standard deviations in the data were: $\sigma_1 = 143$, $\sigma_2 = 1.1$, $\sigma_3 = 1.4$, $\sigma_4 = 16$, $\sigma_5 = 25$, and $\sigma_6 = 2.2$.

The other cases shown used a temperature inside the injection system that was at or above T_c for the pure liquid. Those test cases exhibited no evidence of elastic scattering and we assume there was no intact, thin interface.

Figure 7 indicates that there are characteristic rates of decay in the scattering signal (cases 1, 4 and 5). For subcritical cases, the chamber was hot enough to vaporise the liquid. Even in that case the signal decays, albeit with a long tail. The signal for case 4, however, decays faster and it goes to zero. To ascertain whether one can observe this transition changing axial location and/or rate, we added cases 1a, and 1b. Figure 8 contains curves for those extra cases, together with cases 1 and 4 as well. All four cases had the same subcritical temperature and pressure inside the liquid delivery system; the only difference between the cases was the chamber temperature. Case 1 is for a subcritical chamber temperature ($T_{\text{chamber}} < 170\,^{\circ}C$). The oscillations in the signal and the long tail were a result of Rayleigh breakup, as already explained. The curve for case 1a ($T_{\text{chamber}} = 180\,^{\circ}C$) has evidence for oscillations between 2.5 and 10 *mm*, but past that point the curve decays smoothly to zero. The other two curves ($T_{\text{chamber}} = 200$ and $220\,^{\circ}C$) have few to no oscillations, and they decay more rapidly to zero. These results imply that the interface is weakening, even very near the nozzle, and it happens more rapidly as T_{chamber} increases past $200\,^{\circ}C$. There is a reasonable chance that all of these cases were dominated by evaporation, although the rapid loss of scattering signal as chamber temperature increases implies simultaneous weakening of the interface.

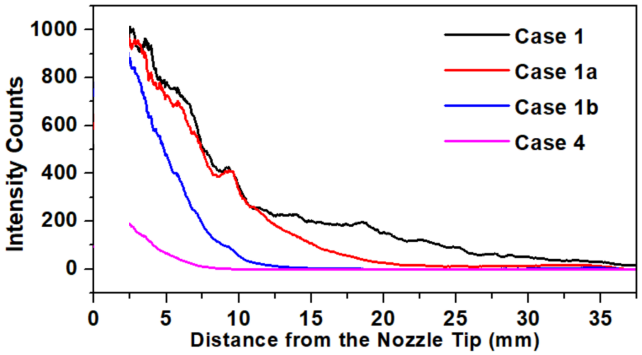

FIG. 8: PELS results with evidence for changes in transition location and rate.

It is important to emphasise that the curves in Figure 8 are based on an average of 200 images, each of which have a spatial resolution of 100 μm, and there was random variation from frame to frame. As the curves drop off to zero, their shape is not representative of a liquid/gas interface. They do indicate, however, that the axial location of transition decreases as the chamber temperature is raised, and the average rate of change increases as well (it is difficult to detect rates in Figure 8, but the case 4 curve does decay more rapidly).

The disappearance of interface scattering is certainly indicative of a vanishing, sharp interface. However, on its own it is not enough to conclude that a thermodynamic transition has taken place. Even in a fully sub-critical case, such as case 1, the signal eventually disappears due to vaporisation. Under conditions designed to create a trans-critical scenario, the interface could vanish both due to vaporising (the initially pure jet is injected at a sub-critical state) and potentially due to 'emission' or diffusion of molecules from the denser main body towards the ambient gas. If an equilibrium, supercritical state is established at some point, it is unclear if that point would exactly coincide with the disappearance of the interface scattering signal. Nevertheless, using a flow time defined based on the jet velocity at the nozzle, we can obtain an estimate of the time required for the interface to vanish.

The jet velocities at the nozzle for cases 1, 4, and 5 were estimated using the known mass flow-rate, the nozzle diameter, and an estimated density at the nozzle provided by FluidProp (density values at the nozzle for all cases are given in the MPLIF section of the results below). The exiting jet velocity for cases 1 and 4 is approximately 1.8 m/s and for case 5 it is 0.5 m/s. Based on these velocity estimates, the jet decay time can be defined as the time required for the averaged ES intensity signal to drop from its peak value to the 20% level. For cases 1 and 4 this time is 7.0 and 2.3 *ms*, respectively. While this estimate is approximate (e.g. the jet velocity is not constant with axial distance) the figures demonstrate that the rate of interface decay increases going from case 1 to case 4, with cases 1a and 1b falling somewhere in between as shown

in Figure 8. The decay in case 5 takes a significantly longer time, estimated to be 51 *ms*. This difference is to be expected since the case 5 jet produces a much lower peak than the jet in case 1, and beyond the 12.5 *mm* location their ES curves have approximately the same slope. The jets in cases 2, 3, and 6 generated no PELS signal and so they were not included in this decay time analysis.

B. PLIF results

Here we present combined PLIF and PELS images for each test case. The PLIF images include one typical transient image together with an average of 100 images. The corresponding elastic scattering data are included for reference.

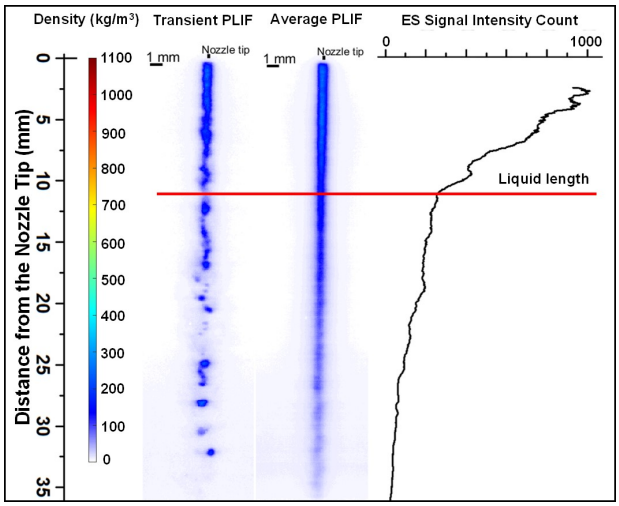

FIG. 9: Test case 1: $T_{\text{Novec}} = 160\,^{\circ}C$ ($T_{r\text{Novec}} = 0.98$), $T_{\text{chamber}} = 150\,^{\circ}C$, and $P_{\text{chamber}} = 16\,bar$ ($P_{r\text{Novec}} = 0.85$). The 12 *mm* liquid length is indicated.

Figure 9 (case 1), for the subcritical case, shows a jet undergoing Rayleigh breakup, a clear sign of surface tension. The chamber temperature induced vaporisation while also modifying the liquid physical properties at the interface.

Figure 10 (case 2) images a superheated vapour jet ($T > T_c$ but $P < P_c$ inside the nozzle). The chamber temperature is below T_c for the mixture. Here the images indicate a moderately dense gas jet at the nozzle outlet; the jet is diffuse and sinuous with no evidence for Rayleigh breakup, and there is no interface scattering signal. Evidence indicates that the jet entered the chamber as a vaporising fluid. The chamber temperature was subcritical, so it is likely that a subcritical vapour would be found around and below the jet (this point is discussed further in the MPLIF results section).

Test case 3 (Figure 11) is very close to the critical point for the pure liquid inside the nozzle and for the chamber. Holding the liquid near the critical point inside the fluid delivery system can produce an instability, although the test case 3 in Table I is stable and reproducible. When operating in the other five test cases in Table I, we found that the liquid control thermocouple was usually less than 10 $^{\circ}C$ lower than the liquid

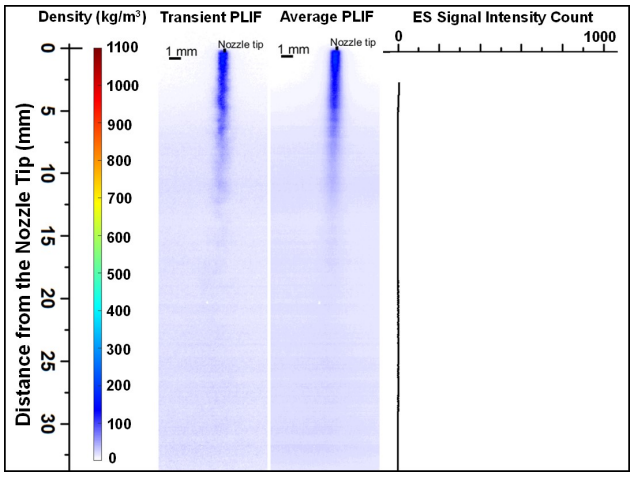

FIG. 10: Test case 2: $T_{\text{Novec}} = 190\,^{\circ}C$ ($T_{r\text{Novec}} = 1.05$), $T_{\text{chamber}} = 150\,^{\circ}C$, and $P_{\text{chamber}} = 16\,bar$ ($P_{r\text{Novec}} = 0.85$).

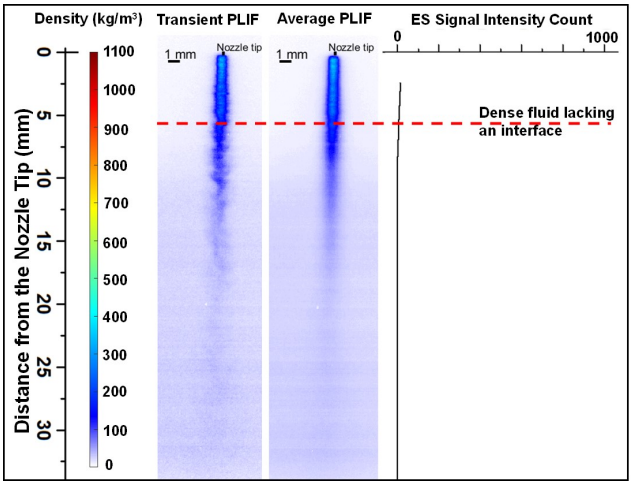

FIG. 11: Test case 3: $T_{\text{Novec}} = 170\,^{\circ}C$ ($T_{r\text{Novec}} = 1.00$), $T_{\text{chamber}} = 170\,^{\circ}C$, and $P_{\text{chamber}} = 19\,bar$ ($P_{r\text{Novec}} = 1.01$).

outlet temperature (there is heater tape wound around the tube in between the control thermocouple and nozzle outlet, so the exit temperature is always higher than the control temperature). For case 3, however, the difference could easily reach 30 $^{\circ}C$ and it could be difficult to stabilise the temperature. This observation is consistent with the findings of Fu and Lin[30], who demonstrate that the thermal conductivity of pure Novec increases rapidly to the critical point, and then just as quickly decreases past the critical point. Figure 11 shows a dense but diffuse, sinuous jet and it contains no evidence for Rayleigh breakup or elastic scattering.

Test case 4 (Figure 12) is for a subcritical pure liquid issuing into a chamber that is supercritical (based upon our VLE estimates). Within the first 10 *mm* the PLIF image shows some very weak wave structure on the jet surface (similar to Rayleigh breakup, but it dissipates with distance) and there is an initial elastic scattering signal. Beyond that axial location, the elastic scattering signal has disappeared and the jet has become diffuse and sinuous before disappearing. Whether

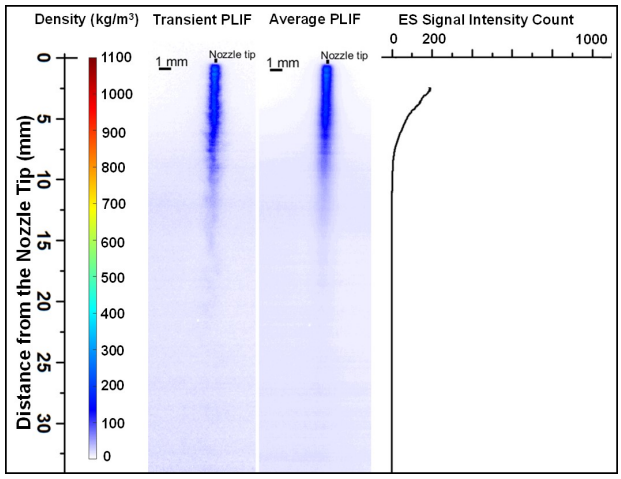

FIG. 12: Test case 4: $T_{\text{Novec}} = 160\,^{\circ}C$ ($T_{r\,\text{Novec}} = 0.98$), $T_{\text{chamber}} = 220\,^{\circ}C$, and $P_{\text{chamber}} = 16\,bar$ ($P_{r\,\text{Novec}} = 0.85$).

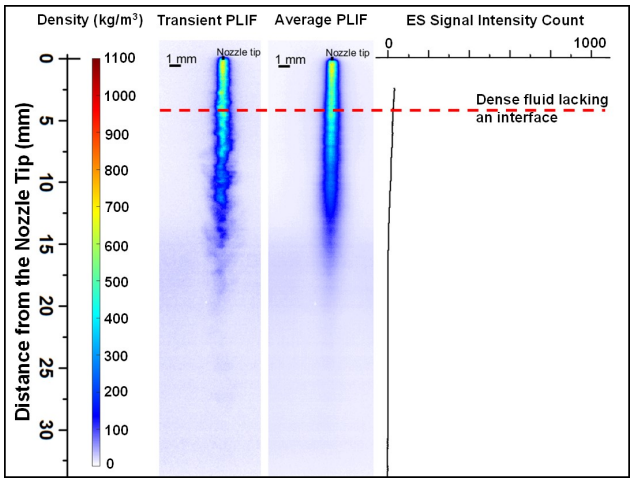

FIG. 14: Test case 6: $T_{\text{Novec}} = 190\,^{\circ}C$ ($T_{r\,\text{Novec}} = 1.05$), $T_{\text{chamber}} = 220\,^{\circ}C$, and $P_{\text{chamber}} = 31\,bar$ ($P_{r\,\text{Novec}} = 1.65$).

the Novec has evaporated or become supercritical is not clear. This jet was discussed further in the section on scattering.

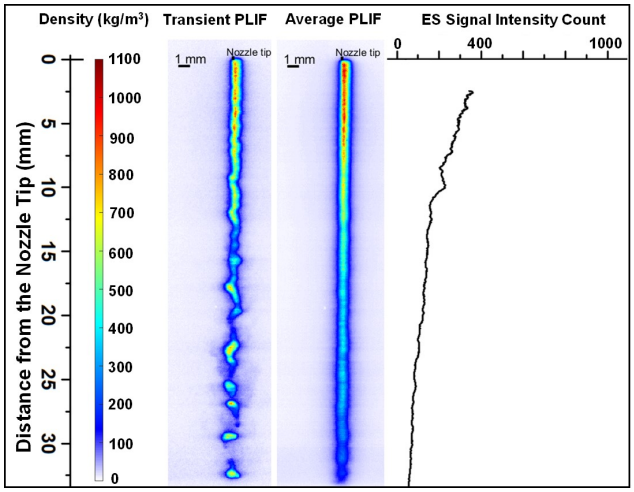

FIG. 13: Test case 5: $T_{\text{Novec}} = 160\,^{\circ}C$ ($T_{r\,\text{Novec}} = 0.98$), $T_{\text{chamber}} = 220\,^{\circ}C$, and $P_{\text{chamber}} = 31\,bar$ ($P_{r\,\text{Novec}} = 1.65$).

Figure 13 contains data for test case 5. During these experiments, the pure Novec inside the nozzle was in the form of a compressed liquid. The chamber conditions were supercritical according to our VLE estimates. The LIF signal is stronger than in the earlier cases because the jet density is higher. This jet is neither supercritical nor is it fully vaporised, because there is clear evidence for surface scattering and the jet is undergoing Rayleigh breakup (with a liquid length around 12 *mm* again). The PELS signal is significantly lower than it was for case 1, however, indicating a weakened interface. The only difference between Figures 12 and 13 is that the data in Figure 13 are for a pressure that is 1.9 times the pressure of case 4 (Figure 12). Here, the Novec boiling point has increased with pressure, significantly reducing the rate of evaporation.

Finally, test case 6 results are shown in Figure 14. Here the pure Novec inside the nozzle was supercritical, while the chamber conditions were also supercritical according to our VLE estimates. The PLIF images imply a jet similar to that of case 5 within the first few *mm*, but it disappears more quickly. The scattering data indicate that there is no well-defined liquid/gas interface.

The injection temperature of the fluid jet appears to have a significant effect on the strength of its interface. For the cases where the injection temperature was below T_c for the pure fluid (for cases 1, 4, and 5) interface scattering could be detected. For the rest of the cases there was virtually no scattering signal even though a dense, gas jet could still be observed via PLIF imaging.

The closest published example similar to our work is the work of Muthukumaran and Vaidyanathan[15], who also studied jets of fluoroketone injected into ambient nitrogen. A direct comparison is difficult owing to differences in the test conditions, mass flow-rates and the fact that they studied an elliptical jet, but there are certain trends in our results that are similar. In the work of Muthukumaran and Vaidyanathan, for the sub-critical cases, Rayleigh breakup was observed. As the injection and chamber temperatures were increased, there was an observed decrease in the jet length and what was a long column of liquid transitioned into a dense gas jet. The more interesting similarity was the increasing presence of a sinuous feature in cases where surface tension came close to vanishing.

In a following study[16], Muthukumaran and Vaidyanathan investigated a round jet, but at a lower fluid reduced temperature of $T_r = 0.68$. The results for these jets injected into nitrogen included evidence for several propagating instabilities that depended on the thermodynamic conditions. These instabilities were not observed in the jets considered here (minimum $T_r = 0.98$), nor were they observed in their elliptical jet study wherein the injection temperature was higher (minimum $T_r = 0.71$).

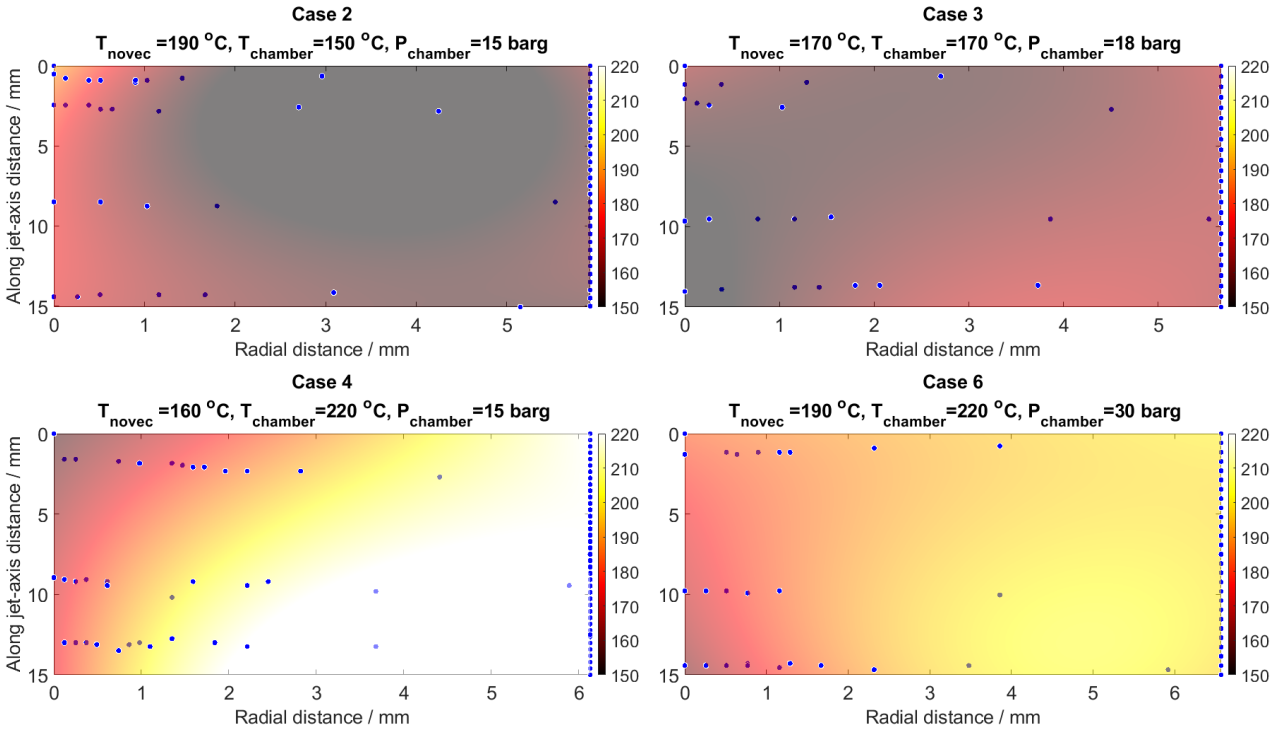

FIG. 15: Temperature results for test cases 2, 3, 4 and 6. The circles in the main body of the diagrams represent measurement locations. There is no difference between the bright blue data points and those that are grey. The grey points appear so because they fell under the fitted surface. Standard deviations of residuals are 5.6, 3.2, 4.3 and 4.1 $^{\circ}C$ for cases 2,3,4 and 6 respectively

C. Temperature results

For both the temperature and MPLIF experiments, test cases 1 and 5 were eliminated because the other conditions presented experimentally more interesting scenarios. The temperature results are shown in Figure 15 as 2-D maps, in which the vertical axes represent the jet-centre axis and the nozzle tip is set as the origin $(0,0)$. The scattered data-points on the main body of the map represent thermocouple measurement locations. The continuous line of points at the right-hand edge of each plot contains artificial data defining a boundary condition calculated as the average of the outermost measurements (radial distance > 5 *mm*), including at axial distances further downstream (not shown here). The maps were created in MatLab using a polynomial ('poly23') surface fit function (the standard deviations of residuals are given in Figure 15).

In case 2, the jet was at a supercritical temperature that was higher than the subcritical chamber temperature. As expected, the jet cooled as it flowed downwards. The ambient temperature was too high to generate detectable condensation of droplets during cooling. Figure 10 shows that elastically scattered light was not detected in this case.

Test case 3 was designed to maintain chamber conditions near the critical point of Novec. The goal was to keep the temperature of both the chamber and the fluid near 170 $^{\circ}C$. Even though the temperature controller was calibrated to inject Novec at that temperature, controlling it very near the critical point was challenging. The data indicate some cooling in the jet with distance. Part of this cooling could be attributed to variations in the measurements themselves together with fluctuations in the injection and chamber temperatures.

In test case 4 the jet was injected at 160 $^{\circ}C$. The expected observation was for the jet to be heated by the significantly hotter chamber (at 220 $^{\circ}C$), and the jet temperature did clearly increase following injection. The disappearance of elastic scattering in Figure 12 occurs at approximately 7.5 *mm*, and a temperature of 172.5 was measured 9 *mm* below the nozzle. The axial distance at which the critical temperature was exceeded and the distance at which elastically scattered light became null, were similar.

For case 6, the expected observation was again for the jet to be heated by the chamber. For this case, both jet and chamber were held at temperatures higher than the critical temperature of the mixture with $T_{chamber} > T_{Novec}$. However, the thermocouple measurements indicated a reduction in temperature near the jet core. This reduction was outside the expected error in thermocouple measurements ($\pm 2.2\,^{\circ}C$). The data were collected over several days and each time the temperature would drop near the jet core. We have not been able to identify a physical phenomenon that would unambiguously explain the observed cooling. Thus, it remains unclear whether there is a physical explanation or if the result is erroneous; caused by the possible adverse effects that a supercritical mixture can have on a physical probe, for example owing to solubility ef-

fects. One explanation could be a change in heat capacity. As discussed previously, the thermodynamic state of Novec inside the nozzle under test case 6 is very close to the Widom line. As the fluid is heated from room temperature to near the pseudoboiling temperature, an increase in the isobaric specific heat capacity is expected. There is a possibility that, because FluidProp using the PC-SAFT model overestimates the critical temperature, the pseudoboiling temperature may also be overestimated. This could mean that the injection temperature might in fact fall to the right of the C_p peak, as shown in the inset plot in Figure 5, in the constant 31 *bar* $C_p(T)$ curve. The significance of this is that a fall in temperature would now be accompanied by a further increase in C_p, facilitating a drop in temperature. Note that at a reduced pressure of $P_r = 1.65$, the increase in C_p is not as profound as it might be at lower reduced pressures, but the detected drop in temperature is also fairly small.

D. MPLIF results

Figure 16 below presents magnified PLIF transient and averaged images. The mixing of the fluid jet with the surrounding nitrogen, and the boundary between them, have been imaged with a spatial resolution of $17\mu m$, providing greater detail. The average images in Figure 16 were corrected as described above but the transient (single) images were not.

In Figure 16, case 2 achieved the shortest core length partly because it was injected as a superheated vapour with the lowest density, and because it has a higher temperature than its surroundings. There is no jet breakup because it is injected as a vapour. According to Figure 15, the temperature remains higher than the critical temperature near the jet axis, even beyond the point where the main jet core has disappeared. Following Banuti's four quadrant portrayal of classical pure fluid states[20], case 2 (for pure Novec) falls into quadrant 2 ($P < P_c$ and $T > T_c$). On the centre-line of the jet, at an axial distance of 8.5 *mm*, the temperature was measured to be 181 $^\circ C$ indicating that the fluid could still be in quadrant 2. By this point, the fluid is no longer entirely pure. However, superheated jets at subcritical pressure depend on diffusional mixing to transition to a mixture supercritical state when injected into fully subcritical conditions. As such, on centre-line and at an axial location of 8.5 *mm*, the mixing of fluoroketone and nitrogen might not have been significant enough for a transition to occur per our VLE estimates. Moreover, by that point the jet would have become aware of the surrounding subcritical pressure (information travel via the speed of sound is faster than diffusional mixing).

Banuti[20] summarised several definitions of the pure fluid supercritical region adopted by various authors. A few of them consider quadrant 2 to be supercritical; others do not (a single phase is not necessarily supercritical). Depending on which definition is chosen, the jet in case 2 could exist as a supercritical fluid during the first few *mm* of its transit. If the requirement is for both P_c and T_c to be exceeded then it is highly unlikely that the fluid (pure or mixture) is supercritical in this case. The transient images show more clearly that the jet enters as a dense, sinuous gas, and the mixing process appears to include significant diffusion.

The flow structure for case 3 was similar to that observed for case 2, albeit with a significantly longer core length. The sinuous characteristic of the jet persists. As with case 2, no elastic scattering was observed, no breakup or ligaments, and the mixing process appears to include significant diffusion. Case 3 is the near-critical case relative to pure Novec where one might have expected much greater fluctuations. However, there are challenges to maintaining a substance at its critical point and the chosen setpoint was one that avoided instabilities by calibrating the controller at a temperature near, but not exactly at, the pure Novec critical temperature of 169 $^\circ C$.

The transient image in Figure 16c contains evidence for surface wave structure at the nozzle outlet (indicating some surface tension), but it dissipates with distance as the jet is heated. Case 4 is the only scenario where occasional droplets were observed. In Figure 16c a drop can be seen at an axial distance just after 12.5mm, and it is clearly distinct from the surrounding vapour. It is possible that this occurred because some Novec fluid remained inside the delivery tube and it condensed. However, such droplets were not observed in case 6, which was tested soon after case 4. It is more likely that droplets appeared because case 4 has a pressure and temperature combination that corresponds to a point very close to the binodal. At an ambient pressure of 16 *bar* the saturated temperature is estimated, through FluidProp, to be 159.3 $^\circ C$, and our injection temperature is set to 160 $^\circ C$. The temperature controller was given a setpoint that ensured the jet evolved into a dense gaseous jet as opposed to a longer column of liquid. Despite the similarities in flow structure and comparable density to cases 2 and 3, case 4 was accompanied by elastically scattered light, that disappears soon after following injection.

The jet in case 6 is injected at a significantly higher density (approximately 740 kg/m^3) than the rest of the cases, giving it higher momentum than the other jets. It extends a longer distance into the chamber before dissipating and, not surprisingly, the transient image contains evidence of shear-based roll-ups along the edge. This structure is characteristic of a dense gas jet, with no surface tension.

Average density profiles for the laser-input side of the jets, found according to the description provided above and at specific axial locations, are shown in Figure 17. The experimental curves on the laser input side (to the right in these images) contain no indication of absorption at the edges, the super-Gaussian fits match nearly exactly there (the average disagreement is on the order of 1 to 2 % with a maximum estimated error of 5 %), and so those edges can be taken to represent reality with very low uncertainty. The locations where absorption begins to have an effect on the PLIF image change with axial distance, and they are indicated by triangles in each plot (the triangles indicate that 5% of the input irradiance has been absorbed at that radius, with absorption levels increasing to the left).

When the correction begins to have a significant effect on the curve, we estimate the combined density scaling uncertainty (based on FluidProp errors, image processing, and LIF

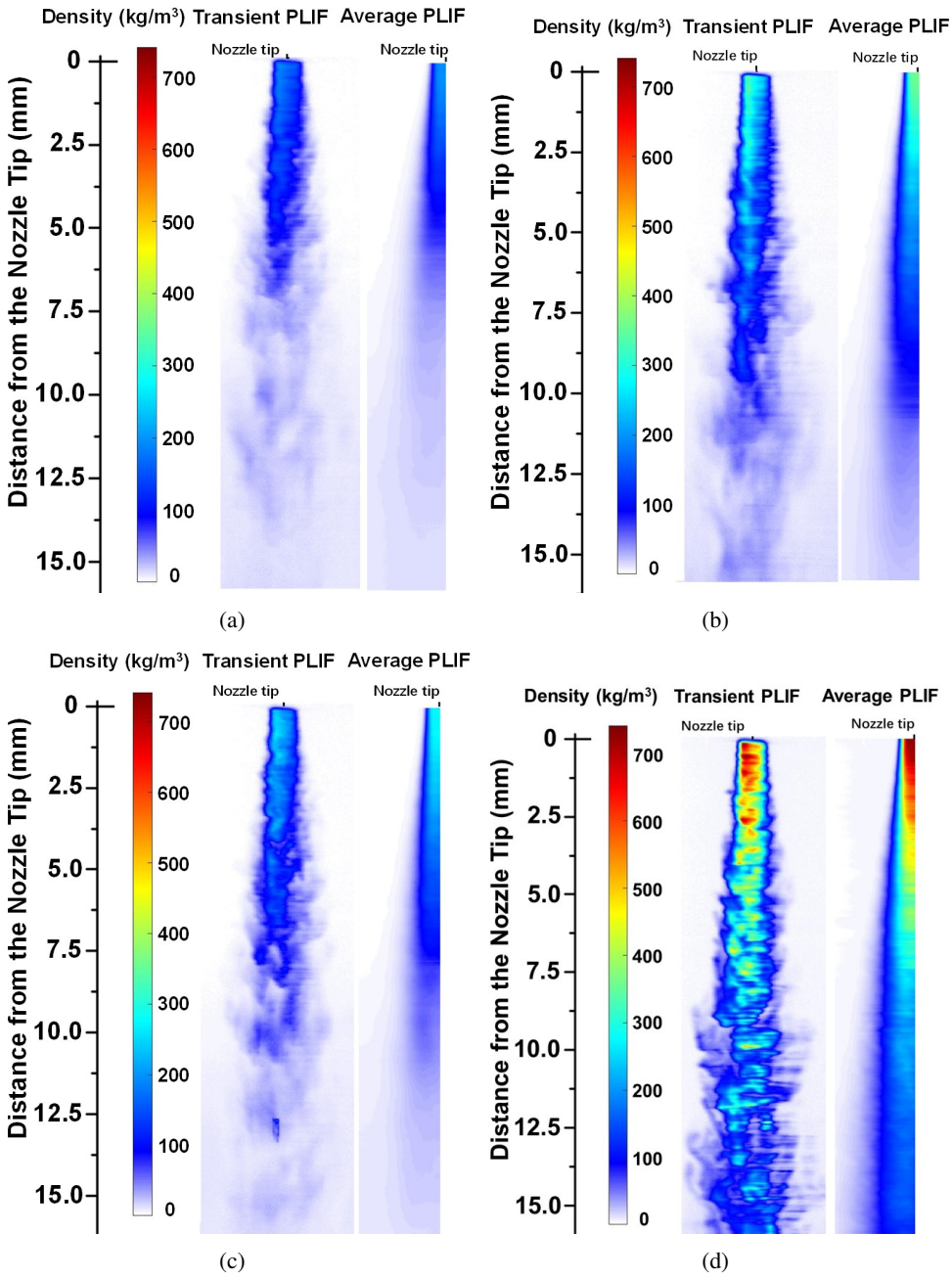

FIG. 16: MPLIF density maps for (a) Case 2, (b) Case 3, (c) Case 4 and (d) Case 6. The laser sheet entered from the left hand side.

scaling) to be 8.1%, 8.5%, 8.9% and 8.9% for cases 2, 3, 4 and 6 respectively. This estimate does not account for the fact that LIF is volumetric, causing more signal in the centre of the cylinder than at the edges. That effect would be difficult to estimate because the laser sheet is thicker than the jet diameter. Dense vapour outside of the interface would also contribute in ways that are difficult to estimate with fidelity. The previously reported 15.4 % disagreement with the mass flow meter at the nozzle is the best indicator of maximum uncertainty.

The super-gaussian parameters for the curves shown in Figure 17, for use in Equation 3, are provided in Table III. If they are of interest, density gradients could be calculated radially from the nozzle centre-line at these axial locations. Close to the nozzle the fitted parameter '*b*' is essentially 0. Further downstream, the centre of the fitted super-Gaussian had to be offset slightly. Values of '*b*' are provided in the table. Note that this offset has been removed in the density profiles depicted in Figure 17, so that all curves are centred at 0.

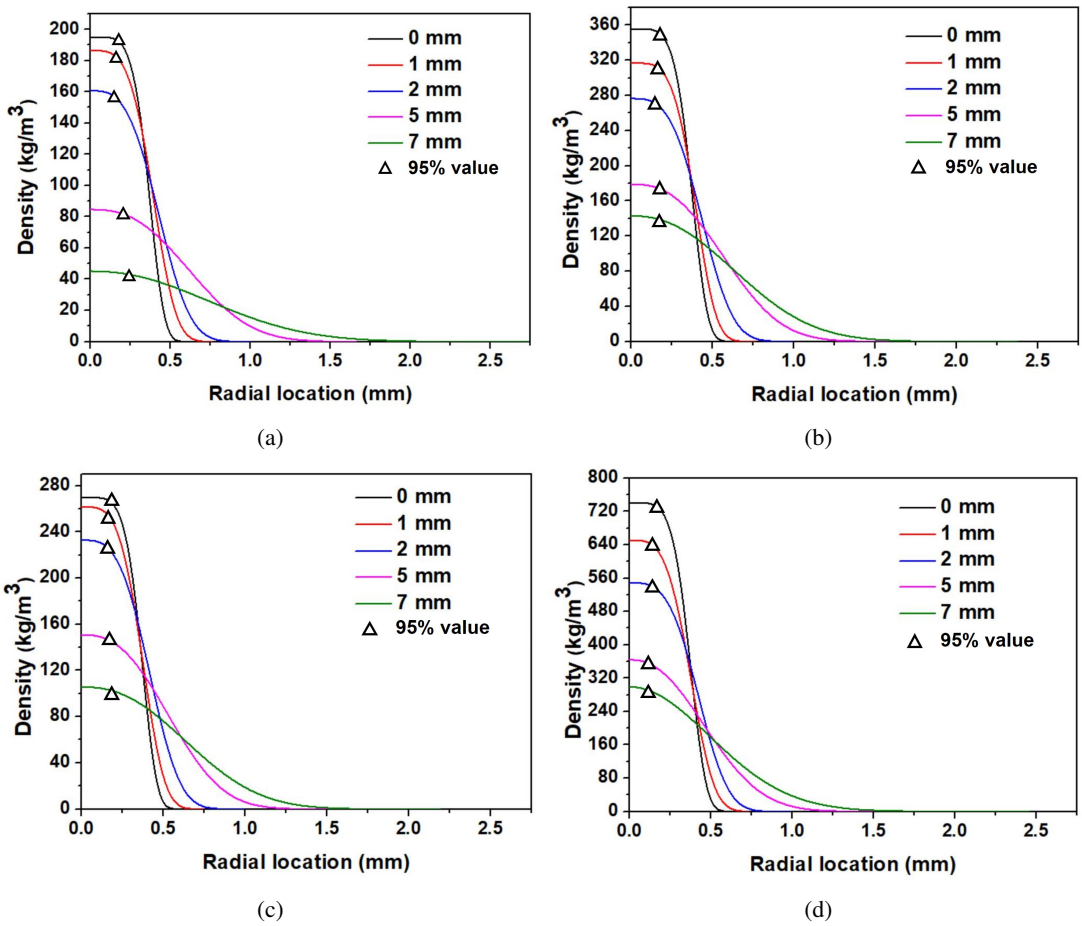

FIG. 17: Averaged Novec density vs radial distance (the laser sheet entered from the right hand side in these plots) for (a) Case 2, (b) Case 3, (c) Case 4 and (d) Case 6. Each line corresponds to a different axial distance. The density at the nozzle was calculated using FluidProp to be 195, 356, 270 and 741 kg/m^3 for case 2,3,4 and 6 respectively

E. Potential evidence for supercritical states

As already mentioned, the disappearance of an interface can be caused either by transition to a supercritical state or by evaporation. The chamber is hot enough to support evaporation, as evidenced by the test case 1, 4, and 5 curves in Figure 7. As liquid evaporates, however, the vapour mixes across the flow-field and the PLIF image of the remaining liquid weakens substantially. Evaporating drops have been observed at axial distances of roughly 40 *mm* below the nozzle exit, under case 1, with no evidence of elastic scattering at that location. The vapour has become a uniform background across the entire chamber (the entire chamber was not viewed here). Some of our test cases do not exhibit those spreading trends and they may contain supercritical regions.

There are regions where the PLIF image indicates a fluid density on the same order as the subcritical density, but there is no evidence for interface scattering. Examples include the regions marked with a red dashed line in Figures 11 and 14. There is a reasonable chance that those datasets indicate a supercritical jet. Case 6 (Figure 14) holds all conditions above the critical point, and if any of our jets were supercritical it would be this one. Those PLIF images indicate a sinuous, dense gas jet. Case 3 could potentially have supercritical locations as well, and as already discussed, case 2 has regions at high temperature that are difficult to categorise.

IV. CONCLUSIONS

This paper has presented a study on interfaces and interface transitions under subcritical, transcritical and supercritical conditions. We have reported spatial and temporal estimates for the destruction of the fluid mixture interface under various conditions. Imaging laser diagnostics for injectant mixture fraction and for the strength of the liquid/gas interface have been applied simultaneously for the first time. The results clearly demonstrate that what appears as an interface in an image captured by an optical system whose spatial resolution is greater than the interface's thickness, is in fact an averaged high density gradient boundary. Important information about the interface is thus inaccessible. This is clearly evidenced by the fact that 'boundaries' which may on face value appear very similar, can in fact differ significantly in terms of

TABLE III: Fitted (density) super-Gaussian profile parameters at chosen axial distances

Case	ρ_{peak} $[kg/m^3]$	N_{peak} $[molec/m^3]$	c $[mm]$	P [-]	b $[mm]$
0 mm from nozzle					
2	195.1	3.72E+26	0.276	2.65	0
3	355.7	6.78E+26	0.280	2.60	0
4	269.8	5.14E+26	0.276	2.70	0
6	741.0	1.41E+27	0.280	2.55	0
1 mm from nozzle					
2	186.4	3.55E+26	0.304	1.95	0
3	316.7	6.04E+26	0.302	2.15	0
4	261.6	4.99E+26	0.288	1.95	-0.02
6	651.1	1.24E+27	0.292	1.85	-0.03
2 mm from nozzle					
2	160.7	3.06E+26	0.341	1.6	-0.02
3	276.3	5.27E+26	0.345	1.65	-0.02
4	232.8	4.44E+26	0.331	1.65	-0.02
6	549.0	1.05E+27	0.335	1.7	-0.02
5 mm from nozzle					
2	84.6	1.61E+26	0.526	1.3	-0.05
3	178.8	3.41E+26	0.484	1.3	-0.05
4	150.8	2.87E+26	0.452	1.3	-0.07
6	364.0	6.94E+26	0.416	1.15	-0.1
7 mm from nozzle					
2	45.1	8.60E+25	0.685	1.1	-0.15
3	142.9	2.72E+26	0.573	1.15	-0.02
4	105.7	2.01E+26	0.563	1.2	-0.08
6	299.1	5.70E+26	0.490	1	-0.13

their fluid interface and its scattering strength.

Some evidence for supercritical states has been acquired. 2-D temperature maps, obtained through measurements with thermocouples and subsequent interpolation, provide useful insight to the steady state condition. There is a significant evolution time once the jet is in the chamber. Moreover, the temperature of the injectant has a bigger effect than does the pressure.

While these results, and this type of experiment when applied to other liquids, can provide useful information, what remains missing is information about the specific thermodynamic state of the fluid. Various properties of the fluid change rapidly at the critical point, and a spatially-resolved measurement of one of these properties could prove immensely useful. In an attempt to make such a measurement, we have applied laser induced grating spectroscopy [(LIGS), also known as laser induced thermal acoustics (LITA), see e.g. Steinhausen et al.[31]] as a measurement of sound speed to this same experiment. We achieved several good quality determinations of sound speed, but the injectant developed a hardened coating on what were new windows only 30 minutes after the start of experimentation. The 355 *nm* wavelength pump laser beams for LITA were set well below the damage threshold for the glass, but they burned the coating and that caused the beams to begin to destroy the glass surface. The laser sheets for PLIF imaging that we used were purposely large, with much less power per unit area, than the requirement for the LITA beams. We did not encounter a similar problem during the PLIF imaging experiments, although the coating was in part responsible for some beam spreading (the WinCam measurements were made with the window in place). Measurement of sound speed will require a redesign of the window arrangement. Alternatively, one could evaluate different LITA setups that use laser pulsewidths, wavelengths, and/or power levels that avoid window damage.

ACKNOWLEDGMENTS

This research was supported by the Air Force Office of Scientific Research (AFOSR) under grant number FA9550-17-1-0129, with Dr. Chiping Li as the technical monitor. It was also funded in part by the UK Engineering and Physical Sciences Research Council (EPSRC) under grant number EP/P011438/1. The authors are grateful to Prof. Piero Colonna at the Technical University of Delft and Dr. Teus van der Stelt at Asimptote for their support developing Novec/nitrogen VLE models.

[1] Z. Falgout, M. Rahm, D. Sedarsky, and M. Linne, Fuel **168**, 14 (2016).
[2] C. Crua, J. Manin, and L. M. Pickett, Fuel **208**, 535 (2017).
[3] L. Jofre and J. Urzay, Prog. Energy Combust. Sci. **82**, 100877 (2021).
[4] J. Bellan, Prog. Energy Combust. Sci. **26**, 329–366 (2000).
[5] J. Bellan, *High Pressure Flows for Propulsion Applications* (American Institute for Aeronautics and Astronautics Inc., Reston VA, 2020).
[6] W. O. Mayer, A. H. Schik, B. Vielle, C. Chauveau, I. Gokalp, D. G. Talley, and R. D. Woodward, Journal of Propulsion and Power **14**, 835 (1998).
[7] B. Chehroudi, D. Talley, and E. Coy, Physics of Fluids **14**, 850 (2002).
[8] R. N. Dahms, J. Manin, L. M. Pickett, and J. C. Oefelein, Proceedings of the Combustion Institute **34**, 1667 (2013).
[9] G. Mo and L. Qiao, Combustion and Flame **176**, 60 (2017).
[10] K. Harstad and J. Bellan, Combustion and Flame **127**, 1861–1879 (2001).
[11] G. Lamanna, C. Steinhausen, F. Weckenmann, B. Weigand, B. Bork, A. Preusche, A. Dreizler, R. Stierle, and J. Gross, in *High Pressure Flows for Propulsion Applications*, edited by J. Bellan (American Institute for Aeronautics and Astronautics Inc., Reston, VA, 2020) pp. 49–110.
[12] B. Bork, A. Preusche, F. Weckenmann, G. Lamanna, and A. Dreizler, Proceedings of the Combustion Institute **36**, 2433– (2017).
[13] V. Gerber, S. Baab, F. Förster, H. Mandler, B. Weigand, and G. Lamanna, Journal of Supercritical Fluids **169**, 105097 (2021).
[14] S. DeSouza and C. Segal, in *High Pressure Flows for Propulsion Applications*, edited by J. Bellan (American Institute for Aeronautics and Astronautics Inc., Reston, VA, 2020) pp. 157–182.
[15] C. K. Muthukumaran and A. Vaidyanathan, Physics of Fluids **27**, 034109 (2015).
[16] C. K. Muthukumaran and A. Vaidyanathan, Physics of Fluids **28**, 074104 (2016).
[17] M. Linnemann and J. Vrabec, Journal of Chemical and Engineering Data **62**, 2110–2114 (2017).
[18] M. O. McLinden, R. A. Perkins, E. W. Lemmon, and T. J. Fortin, Journal of Chemical and Engineering Data **60**, 3646–3659 (2015).
[19] J. Bellan, Combustion Science and Technology **178**, 253 (2006).
[20] D. Banuti, M. Raju, P. Ma, and M. Ihme, "Seven questions about supercritical fluids - towards a new fluid state diagram," AIAA SciTech Forum, American Institute for Aeronautics and Astronautics (2017).
[21] M. Raju, D. Banuti, P. Ma, and M. Ihme, Nature Scientific Reports **7**, 3207 (2017).
[22] G. G. Simeoni, T. Bryk, F. A. Gorelli, M. Krisch, G. Ruocco, M. Santoro, and T. Scopigno, Nature Physics **6**, 503 (2010).
[23] D. T. Banuti, Journal of Supercritical Fluids **98**, 12 (2015).
[24] T. M. Koller, T. Klein, C. Giraudet, J. Chen, A. Kalantar, G. P. van der Laan, M. H. Rausch, , and A. P. Fröba, J. Chem. Eng. Data **62**, 33193333 (2017).
[25] S. Yang, G. Kasapis, and M. Linne, Experiments in Fluids **63** (2022), DOI:10.1007/s00348-022-03492-9.
[26] M. Linne, *Spectroscopic Measurement: an Introduction to the Fundamentals* (Academic Press, Amsterdam, 2002).

[27] W. Mayer, J. Telaar, R. Branam, G. Schneider, and J. Hussong, Heat and Mass Transfer **39**, 709 (2003).
[28] J. P. R. Gustavsson and C. Segal, *Characterization of a Perfluorinated Ketone for LIF Applications*, Tech. Rep. (American Institute of Aeronautics and Astronautics, 2008).
[29] A. Roy, *Subcritical and supercritical fuel injection and mixing in single and binary species systems*, Ph.D. thesis, University of Florida (2012).
[30] B.-R. Fu and W.-J. Lin, International Communications in Heat and Mass Transfer **117**, 104740 (2020).
[31] C. Steinhausen, V. Gerber, A. Preusche, B. Weigand, A. Dreizler, and G. Lamanna, Experiments in Fluids **62** (2021).